A personalised computational model of the impact of COVID-19 on lung function under mechanical ventilation

Jason M. Carson, Raoul Van Loon, Hari Arora *

Department of Biomedical Engineering, Faculty of Science and Engineering, Swansea University, Bay Campus, Fabian Way, Swansea, SA1 8EN, Wales, UK

ARTICLE INFO

ABSTRACT

This work proposes a modelling framework to analyse flow and pressure distributions throughout the lung of mechanically ventilated COVID-19 patients. The methodology involves: segmentation of the lungs and major airways from patient CT images; a volume filling algorithm that creates a dichotomous airway network in the remaining volume of the lung; an estimate of resistance and compliance within the lung based on Hounsfield unit values from the CT scan; and a computational fluid dynamics model to analyse flow, lung inflation, and pressure throughout the airway network. Mechanically ventilated patients with differing progression and severity of the disease were simulated. The results indicate that the flow distribution within the lung can be significantly affected when there are competing types of lung damage. These competing types are primarily fibrosis-like lung damage that creates higher resistance and lower compliance in that region; and emphysema, which causes a decrease in resistance and increase in compliance. In a patient with severe disease, the model predicted an increase in inflation by 33% in an area affected by emphysema-like conditions. This could increase the risk of alveolar rupture. The framework could readily be adapted to study other respiratory diseases. Early interventions in critical respiratory care could be facilitated through such efficient patient-specific modelling approaches.

1. Introduction

The COVID-19 pandemic, caused by the severe acute respiratory syndrome coronavirus 2 (SARS-CoV-2), has been a factor in millions of deaths worldwide. COVID-19 put healthcare systems under enormous stress. The majority of people infected by the virus have relatively mild symptoms. However, the risk of severe disease increases significantly with co-morbidities. This includes cardiovascular diseases, diabetes, chronic kidney disease, cancer, and obesity [1]. In addition, people that initially presented with mild disease are at risk of developing other symptoms post-recovery, often termed as long-COVID [2,3]. The SARS-CoV-2 virus has been shown to interfere with many body organ functions, including the lungs, heart, blood vessels, brain, and kidneys.

One of the more serious complications is pneumonia [4], which can cause pleural effusion (fluid infiltration of the lungs) and diffuse alveolar damage, leading to a reduction in lung function. This can reduce gas exchange, which can lower blood oxygen levels, and increase carbon dioxide levels. COVID-19 pneumonia can develop into acute respiratory distress syndrome (ARDS) and cause respiratory failure. When a patient fails to respond to non-invasive intervention, invasive mechanical ventilation (IMV) is required. IMV can save lives, but can also lead to ventilator-induced lung damage [5,6], which would further

interfere with airflow and pressure distributions in the lung. In order to reduce the amount of lung damage caused by IMV, it is important to try and tailor the mechanical ventilator settings to the individual patient needs [7]. A clinical trial found that using continuous positive airway pressure (CPAP) can reduce the need to put the patient under IMV [8].

The link between underlying mechanical change due to disease and the global lung response is poorly understood. All current work in this area has been performed on rodents, which may not be applicable to understanding human respiratory responses. A study used rodents on mechanical ventilation to understand how volumetric strain and pressure-volume loops change due to traumatic injury [9]. The damaged lung showed a wider distribution of volumetric strain which indicated that after damage, the airflow distribution changed significantly compared to healthy lungs. Another study used high fidelity micro-CT imaging on rodent lungs under mechanical ventilation to develop a more accurate comparison of local volumetric lung tissue strains and global lung mechanics [10]. Digital volume correlation has been utilised in combination with pressure-volume data to investigate local strain data with global lung response [11]. More recently, digital image correlation has been used to compare local strains between healthy and diseased rodent lungs [12].

---

* Corresponding author.
  E-mail address: hari.arora@swansea.ac.uk (H. Arora).

Understanding of the branching structure of airway networks was significantly improved following the works of Weibel and Horsfield [13–15]. Generally only the first few branching generations of airways can be segmented from a medical image. For smaller airways, several volume-filling algorithms have been developed to create 3-dimensional airway networks within the bounds of lungs. The majority of works use the following two studies as a basis:

- Kitaoka et al. [16] - use purely deterministic algorithms to split the lung volume into smaller regions and create new airway branches. The method is a top-down approach, which starts with the largest airways and then generates smaller branches until terminal regions have been reached. An algorithm with a similar top-down process was also presented in [17].
- Tawhai et al. [18] - the method begins with an initial randomisation of points within a lung volume that represent terminal regions. An algorithm that uses these random points then extends the network from the largest airways, down to the terminal regions. Rules are in place to determine if any branching pathway should be terminated. The diameter of the created branches are also randomised within a bound. The algorithm can be considered a bottom-up approach as it uses the randomised terminal points to guide the creation of airways. Extensions to this method have been developed or utilised in several studies [19–21].

Previous computational fluid dynamics models have been performed on airflow in the lungs, generally focusing on the upper airways [22,23]. Other studies include analysing the structure and function of asthmatic lungs [20], and airflow in pulmonary acinus idiopathic interstitial pneumonia [24]. Reduced-order 0-dimensional models have been used to investigate global lung function [25]. In [26], a 0-dimensional fluid flow model is used with non-linearly compliant walled airways and acinar units to model the effect of surfactant distribution on pressure and flow distributions in the lung. Another study utilised 1-dimensional modelling for the larger airways with an assumption of rigid walls. The acinar units (collection of alveoli) are treated in two different ways in separate models. One model defines the pressure directly within the acinar units as a boundary condition; while the other model defines the pressure in the pleural cavity with an assumption that the acinar units have static compliance [27].

An airflow model of COVID-19 was developed to analyse flow and pressure distributions in tidal (normal) breathing [28]. In their model, the larger airways (up to generation 16) are treated as rigid 0-dimensional structures. The acinar units are lumped models with a non-linear compliance based on surfactant concentration which change due to the CT scans radiodensity measure (Hounsfield units). This means that the model lacks an estimation of compliance and resistance changes from other sources, such as the chest wall. In addition, the use of a 0-dimensional model for the airflow mean that wave-propagation phenomena cannot be captured. A poro-elastic model has been developed of the whole lung [29] and showed good agreement with global measures of volume and pressure. However, such a model would struggle at capturing local effects and wave-propagation phenomena. This is because the airways are not porous media, and are instead a directed network of airways with a unique pathway from one location in the lung to another. More recent efforts in the area of full lung respiratory modelling include the investigation of aerosol deposition [30,31] and multi-scale modelling of normal breathing [32,33].

1.1. Motivation and contributions

Recent advances have been made in area of respiratory modelling, though several gaps remain. Currently, to the authors knowledge, no respiratory models exist that include the following combination of important attributes for understanding lung function of an individual under mechanical ventilation.

- A framework that investigates the local and global impact of invasive mechanical ventilation of flow and pressure distribution throughout the lungs. The ability to capture local and global phenomena provides the capability to efficiently interrogate any at risk regions.
- The utilisation of patient imaging techniques to personalise a computational model of the respiratory system.
- The implementation of a computational methodology that can analyse non-linear wave propagation phenomena.

To address the above research gap, this study presents a comprehensive computational framework to model the airflow, pressure, and inflation of structures throughout the lung under invasive mechanical ventilation. This could improve the estimation of alveolar rupture risk, and the locations within the lung that may be most vulnerable to rupture for a given patient. The model incorporates patient CT images into the framework to personalise the model and analyses the impact of different disease types and distributions within the lung.

The main contributions of this work include:

- the development a global airflow model of the lung that includes the primary bio-mechanical processes involved in invasive mechanical ventilation;
- the use of patient respiratory CT images to create a personalised airway networks;
- a framework to estimate major airway parameters and their distribution in the lungs, from a 'healthy' state to a pathological, mechanically ventilated lung;
- the use of computational fluid dynamics to investigate airflow and pressure distributions within a structured airway network for a mechanically ventilated lung.

2. Methodology

An overview of the framework is shown graphically in Fig. 1. The first step of the framework involves the analysis and segmentation of computed tomography pulmonary angiography (CTPA) images to extract the geometry of the lung boundaries and major airways. The second step utilises a network generation algorithm to extend the segmented major airways. This creates a dichotomous airway tree that fills the lung volume down to the terminal bronchioles. A computational fluid dynamics (CFD) model is used to predict the airflow and pressure distribution within the compliant airways of the lung. The model consists of a one-dimensional deformable network for the upper airways, while 0-dimensional models are used to model the highly compliant alveolar structures. In order to reduce the number and uncertainty of model parameters, several assumptions are made. This includes disregarding the complicated interaction between a patients spontaneous breath and the mechanical ventilator settings. In this work, it is assumed the patient would be in a medically induced coma under mechanical ventilation, and thus the patient does not trigger the beginning of inspiration (the ventilator is in control mode). This means the inlet boundary condition of the computational fluid dynamics model (trachea) is set to standard volume-controlled ventilator settings.

2.1. Data acquisition and segmentation

Patient data has been acquired during routine clinical practice in the treatment of COVID-19 patients within the Hywel Dda University Health Board, Wales, UK. All required ethics where obtained before commencing this work and all required ethic procedures were followed. The patient data has been de-identified prior to being shared with the researchers on the project to ensure data protection is respected. A data-sharing agreement is in place between the institutions involved in this work to ensure the standard practice for data handling and storage are followed. Table 1 shows an overview of the two patients, including their co-morbidities. Patient 1 had milder disease although
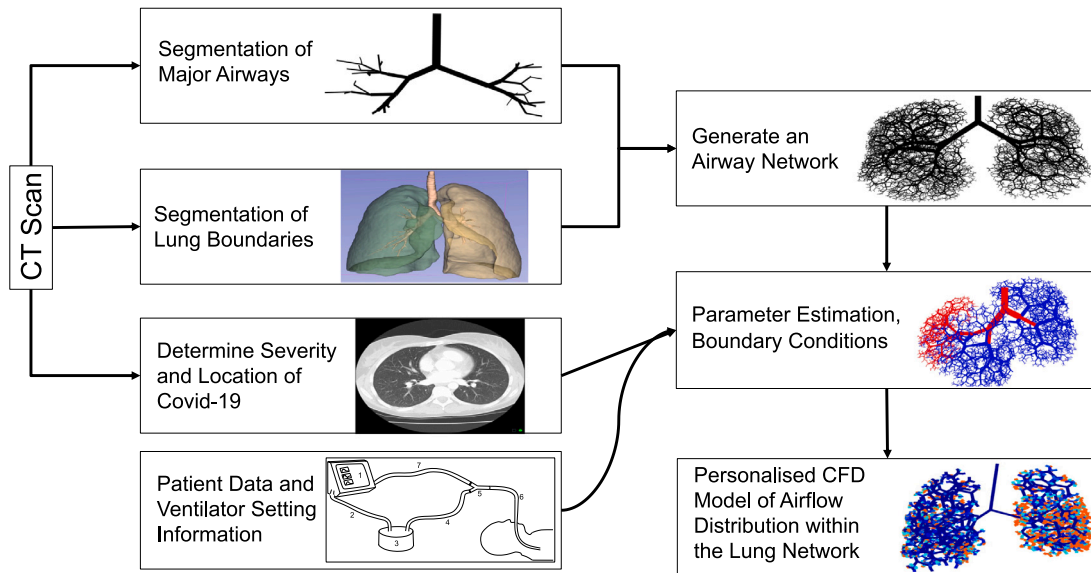
Fig. 1. Overview of the framework which shows the link between each part of the workflow to produce the final computational fluid dynamics (CFD) simulation results. The graphic shows where the patient data is utilised within the modelling methodology and how the sub-components of the framework fit together.

Table 1
Overview of the patients which includes sex, age, and co-morbidities. ILD is interstitial lung disease, and COPD is chronic obstructive pulmonary disease.

	Patient 1	Patient 2
Sex	F	F
Age	47	86
Co-morbidities	Hypothyroidism,	ILD
	Arthritis,	COPD
	Chronic Fatigue Syndrome	Breast Cancer

still required admission to hospital . Patient 2 had much more severe disease caused by COVID-19 and had more serious co-morbidities.

Segmentation of CTPA images are performed in 3D Slicer (https://www.slicer.org) following a semi-automated approach using the Lung CT Analyser project to create an initial mask (https://github.com/rbumm/SlicerLungCTAnalyzer). A researcher experienced in medical image segmentation performed additional manual editing of the segmentation to correct errors that had been created in the initialisation stage. The lung volume and major airways are segmented, the centreline information of the major airways are then extracted using the vascular modelling toolkit (http://www.vmtk.org/) to create a network of airways in terms of the airway diameters, and the first and last nodal positions of each airway in 3d space. This allows the construction of a 1D network from the segmented airways, which are used as a basis for generating the remainder of the airway network.

2.2. Network generation algorithm

The segmented lung volume, together with the geometric information of the segmented airway network, are used as the initialisation state for the network generation algorithm. The algorithm primarily follows the set of rules by [16] to create a dichotomous tree, with some modifications that ensure optimal filling of the entire lung volume with airways. Due to these modifications, the algorithm utilised in this work is described in full in the supplementary file accompanying this manuscript to ensure clarity and reproducibility.

The main assumptions and outcomes of the network generation are the following. The network created is determined from a set of rules founded on literature based measurements that: restrict airway length and diameter; use bifurcation relationships such as the branching angles of child airways; and split a volume into two smaller sub-regions.

The algorithm continues to propagate a branching pathway of the airway network until one of two main conditions are met. Firstly, that an airway reaches a boundary, which could be the lung boundary, or the boundary of the region to which it supplies air. Secondly, the algorithm terminates if a user-defined minimum regional sub-volume tolerance is reached for that pathway. An important assumption of the algorithm is that the amount of flow that is distributed to each child airway of a bifurcation is proportional to the respective diameters of those child airways. This means than the child airway with the largest diameter, will supply air to a larger sub-region. As a result of this inherent assumption, the network generation algorithm automatically gives an initial estimation of the resistance and compliance distribution within the lung. Although the resistance and compliance values are then adapted based on the local Hounsfield Units, which is described in Section 2.4.2.

2.3. Computational fluid dynamics

2.3.1. 1D physics-based model - trachea through to respiratory bronchioles

The governing equations employed in this work are the incompressible Navier–Stokes equations reduced to one dimension. The assumptions used in this work are that an airway has an axial symmetry, only radial wall displacement occurs in an airway, pressure is constant within a cross-section, and the axial velocity component of the airflow is the most dominant, thus allowing for circumferential and radial velocity components to be neglected. This results in the following governing equations in a pressure and flow rate formulation. The continuity equation is given as,

$$C\frac{\partial P}{\partial t} + \frac{\partial Q}{\partial x} = 0, \tag{1}$$

and the conservation of linear momentum as,

$$\frac{\rho}{A}\frac{\partial Q}{\partial t} + \frac{\rho}{A}\frac{\partial \left(\frac{Q^2}{A}\right)}{\partial x} + \frac{\partial P}{\partial x} + \frac{\tau\mu\pi Q}{A^2} = 0. \tag{2}$$

where C is the airway wall compliance, P is the pressure, Q is the flow rate, A is the cross-sectional area, t is the temporal coordinate (time), x is the axial spatial coordinate, μ is the dynamic viscosity of air, ρ is the density of air, and $\tau = 22 \text{ cm}^2/\text{g}$ is the viscous friction coefficient. The final equation that is required to solve this system of equations is the constitutive law that provides the relationship between pressure and

area. The constitutive law used is the following non-linear power-law model with a Kelvin-Voigt visco-elastic term [34],

$$P - P_{ref} - P_{ext} = \frac{2\rho c_{ref}^2}{b}\left(\left(\frac{A}{A_{ref}}\right)^{b/2} - 1\right) + \Psi_{visc}, \qquad (3)$$

where $P_{ref} = 5\text{cmH}_2\text{O}$ is the reference pressure, A_{ref} is the area at the reference pressure,

$$b = \frac{2\rho c_{ref}^2}{P_{ref} - P_{collapse}}, \qquad (4)$$

and the contribution of the wall viscous term,

$$\Psi_{visc} = \frac{\gamma}{A_{ref}\sqrt{A}}\frac{\partial A}{\partial t}. \qquad (5)$$

The wave speed c_{ref} is calculated based on the radius at the reference pressure r_{ref} as:

$$c_{ref} = \sqrt{\frac{2}{3\rho} * (k_1 * \exp(k_2 * r_{ref})) + k_3}, \qquad (6)$$

with $k_1 = \{150\,000, 30\,000\}$, $k_2 = \{-1.8, -1\}$, and $k_3 = \{33\,700, 2800\}$, for the stiffer airways (trachea, bronchi) and more compliant bronchioles, respectively. The collapse pressure is $P_{collapse} = -13.6\text{cmH}_2\text{O}$. The format of Eq. (6) is chosen to be the same as that presented for blood vessels [35] but with modified values to achieve a physiologically sensible distribution of compliance to the larger airways. This process achieves a compliance distribution of 10% of the total lung compliance from the trachea to the terminal bronchioles, while the remaining 90% is distributed to the lumped models that represent the remainder of the network. This estimation of compliance distribution is chosen to follow the volume distribution found in [36].

The viscous term is calculated for all 1D branches as:

$$\gamma = \frac{100}{D} + 400, \qquad (7)$$

where D is the branch diameter [34].

The tissue composition of the branch wall changes depending on location. More cartilage is generally present in the walls of the trachea. Moving further down the network, the amount of cartilage reduces, while the amount of smooth muscle increases. The walls of the bronchioles contain almost no cartilage, and are primarily composed of smooth muscle. Thus the compliance of each airway generation in the network tends to increase as the location changes from trachea through to the terminal bronchioles, respiratory bronchioles, and alveoli.

In this work, two different parameter estimations of the constitutive laws are considered for the lung branches to cover the two main structure types. These are: (1) the more rigid trachea and (2) the more compliant-walled bronchioles through to the terminal bronchioles. Fig. 4(b) compares the constitutive wall behaviour of the trachea, and a large and small bronchi. The radial strain to pressure relationship can be observed to exhibit a similar behaviour to experimental measurements by [37].

The system of equations are solved using a second-order backward difference discretisation for time and a sub-domain collocation scheme in space that was developed and validated for haemodynamics [38,39].

2.3.2. 0D physics model - respiratory bronchioles and alveolar structures

The ends of the 1D network are connected to three-element Windkessel 0D lumped models and is illustrated in Fig. 2. This is comprised of: a characteristic impedance (resistance) to minimise artificial wave reflections; a second resistance that represents the effect of the remainder of the downstream resistance of the pulmonary airway network, which includes the resistance to airflow from the chest wall; and a compliance element which represents the remaining downstream compliance of the system, including the alveolar structures and chest wall. The lumped model represents the lower airways, which begin at the level of the respiratory bronchioles and end with the pulmonary

acinar units. The resistance and compliance elements can be expressed as:

$$\frac{1}{R}(\Delta P) = Q_R, \qquad (8)$$

$$C_a\left(\frac{\partial P}{\partial t} - \frac{\partial P_{ext}}{\partial t}\right) = Q_{Ca}, \qquad (9)$$

where R is the resistance, C_a is the compliance, ΔP is the pressure difference across the resistance, Q_R is the flow rate across the resistance, and Q_{Ca} is the flow rate within the compliance element.

The final equation required is the constitutive relationship, which will give the relationship between the wall stress (in this case pressure), and the wall strain (in the 0d model, using the volumetric strain). The non-linear power law model with a Kelvin-Voigt visco-elastic term,

$$P - P_{ref} - P_{ext} = \frac{2\rho c_{v,ref}^2}{b_v}\left(\left(\frac{V}{V_{ref}}\right)^{b_v/2} - 1\right) + \Psi_v, \qquad (10)$$

where V, and V_{ref} are the volume and reference volume of the alveoli. The $c_{v,ref}^2$ and b_v are used as free model parameters for tuning towards pressure-volume relationships and total respiratory compliance values from literature [40]. If a patient pressure-volume loop is measured, then the patient measurement data could also be utilised to estimate $c_{v,ref}^2$ and b_v in local regions of the lung. The viscous term is,

$$\Psi_v = \frac{\gamma_v}{V_{ref}\sqrt{V}}\frac{\partial V}{\partial t}. \qquad (11)$$

V, and V_{ref} are the volume and reference volume of the alveoli. With the assumption that 90% of the lung compliance is in the terminal structures, the reference wave speed is calculated to be $c_{v,ref} = 5000\text{cm/s}$ and the power term is $b_v = 9.7$. These are found using a parameter estimation technique with assumptions of alveolar number as described in Section 2.4.1. The viscous term is calculated to be $\gamma_v = 0.001$. While the viscous effect of one alveolus is small, the cumulative effect of the viscous term is significant and adds to a noticeable hysteresis in the pressure-volume loop.

2.4. Parameter estimation and boundary conditions

The inflow at the top of the trachea is set to resemble a volume curve of a volume-controlled mechanical ventilator setting with a tidal volume of 0.5 L, where the respiratory period is set to 4 s. The inflow condition is shown in Fig. 3. The 1d terminal bronchioles are connected to a three-element Windkessel model to represent the downstream respiratory bronchioles and alveolar structures. The resistance and compliance in the model are modified by the Hounsfield units of the CT scan in order to investigate the effects of COVID-19 distribution on the mechanical function of local regions within the lung. The initial resistance distribution is determined by the network generation algorithm.

2.4.1. Parameter estimation of alveoli compliance - alveoli wall model

The number of alveoli in the entire lungs is approximately 300–780 million alveoli. In this work, it is assumed that the lung is filled with 170 alveoli per cubic millimetre as found by [36] of lung parenchyma. Furthermore, the same study found that lung parenchyma filled approximately 92% of the total lung volume of 1534 ml, alveoli covered about 70% of the lung parenchyma. This means that alveoli fill approximately 64% of the total lung by volume. It was also observed that each alveolus is approximately 4.2×10^{-6} ml.

Although these values are extremely useful as a basis for the model proposed in this work, it should be noted that the study by [36] used lung fixation ex-vivo with a liquid solution, and a comparison between the total lung capacity derived from CT and the lung volume measured during ex-vivo fixation has never been performed. In this work the lung volume is derived from the segmentation of a patient CT scan. This will generally require the patient to hold their breath at full inhalation,
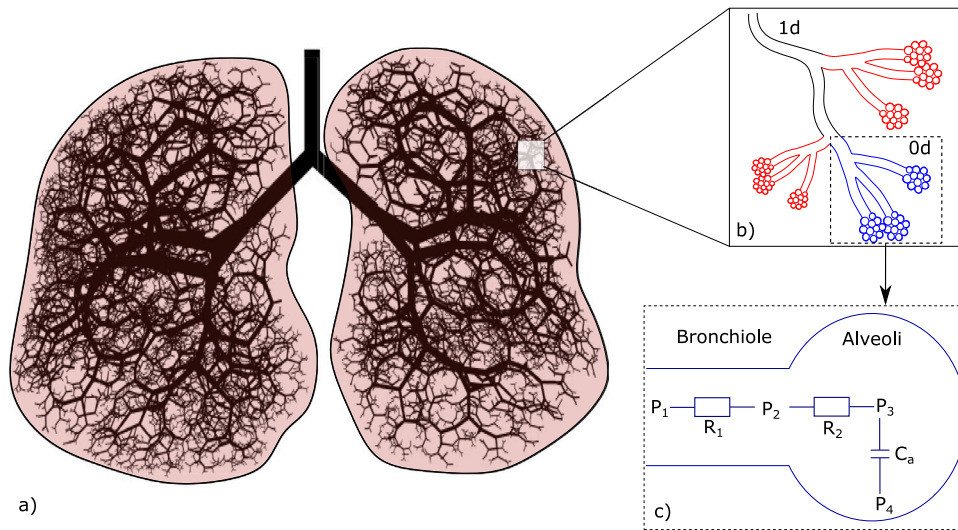
Fig. 2. Overview of the 1d-0d network. (a) is an example 1d network from patient case 1 (mild disease), (b) is an example of how the 1d and 0d models are connected, and (c) is an example of one lumped model that represents the downstream compliance (C_a), characteristic impedance (R_1), and a combined resistance of: respiratory bronchioles through to the alveoli and the chest wall (R_2). The lumped models that represent the lung structures responsible for gas-exchange are composed of two resistors and a capacitor.
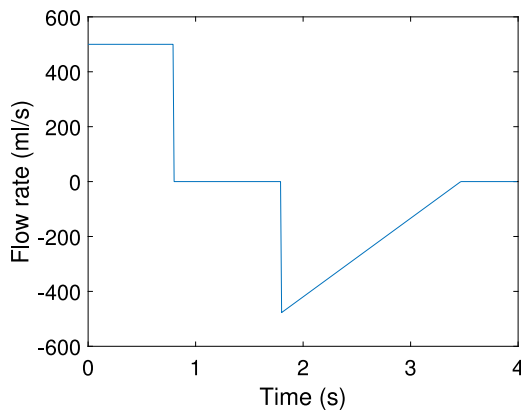
Fig. 3. Inflow waveform for the CFD simulations.

which would ideally be 100% of total lung capacity (TLC). However, this is not the case in reality as: the patient is ill and is likely to have their breathing function impaired which would lower their ability to inhale fully, thus would not be performed at TLC; and the patient would typically be in the supine position, which also lowers their TLC [41].

In this work the following is assumed in order to estimate the number of alveoli in the lung: The patient CT is assumed to be at total lung capacity, which as an example in the mild disease case, gives a segmentation volume of 2873 ml for the right lung and 2676 ml for the left lung. It is assumed that the alveoli cover 64% of the lung volume from [36]. This gives a total volume of alveoli in the right lung to be 1839 ml, and 1713 ml in the left lung. Assuming that the volume of an alveolus is 4.2×10^{-6} ml, the total number of alveoli in the right lung is estimated to be 312,630,000 and in the left lung is 291,210,000. The final assumption is that the alveoli are chosen to be uniformly distributed within the lung volume. The compliance of the lung is also distributed uniformly throughout the volume as an initial estimate. The assumptions in the network generation algorithm creates a collection of terminal sub-regions with a known volume. This means that the number of alveoli and compliance of each 0D terminal model are initially estimated from the network generation algorithm. Although the distributions of both the compliance and resistance are then adapted depending on the Hounsfield unit distribution from the CT scan.

2.4.2. Extract Hounsfield units from image

The Hounsfield units (HU) are extracted for each region in the lung volume and are shown in Figs. 5(a) and 5(b). HU in healthcare are typically saved in 12-bit format, and thus have a range of 4096. This range is between −1024, which represents air, through to 3071, which represents tooth enamel, which is the most dense material in the human body. Higher values of HU units are possible, but are generally not of interest in healthcare. Although HU units are useful for highlighting anomalies within the body, significant variation of HU units can be observed depending on the protocol and reconstruction parameters, with variations of up to 39.4% [42] observed in literature. A variation of 25.6% was seen in HU values in denser materials, while it is much lower for materials with density of less than 1.1 g/cm³, where a variation of 2.6% was observed [43]. Although greater variation in HU values are observed in obese and overweight individuals [44]. Material densities of 1.1 g/cm³ approximately correspond to 100 HU, and as the lung parenchyma along with any fluid build-up in the lung are below 100 HU, no HU unit normalisation or correction is performed in this work.

Generally the normal healthy HU range of a lung is −1024 HU to −700 HU with a mean around −850 HU. Emphysema will push the HU unit mean down towards −900 HU and also decrease the statistical measure of kurtosis. A study found the mean HU in patients with a healthy lung to be −739 HU, while the mean for an idiopathic pulmonary fibrosis (IPF) group was −596 [45]. In addition, the kurtosis and skewness of the HU distribution was significantly reduced in the IPF group.

With this in consideration, the scaling of resistance and compliance is calculated in the following way. The HU values are averaged in each sub-volume that have been created from the network generation step that includes all 23 generations of airways. Any point with a HU value of greater than 500 is assumed to be lung tissue that is not inflated with air, such as blood vessels, and are excluded in the HU averaging process in the sub-volume. The calculation of the scaling term S is defined as a piecewise linear function with coordinates in the HU range $[-1024, 3071]$. The function can be seen in Fig. 4(a). The points chosen are primarily trying to mimic the change in resistance due to the impact of fluid build-up and tissue damage. A small increase is chosen between an HU of −1024 and −500 as it may indicate some fluid in the lung towards the HU of −500. The range HU −500 to −100 indicates significant fluid within the lungs which will reduce the lumenal area of the airways and increases the resistance to airflow. For
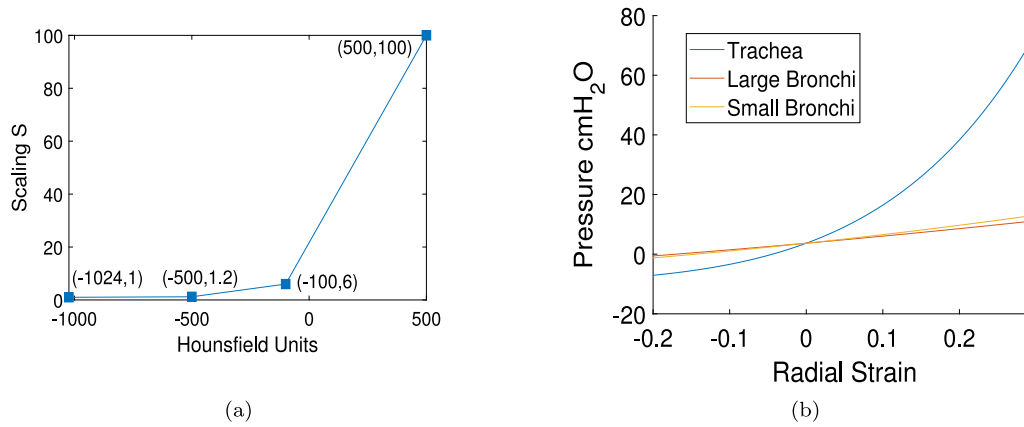
Fig. 4. Compliance and resistance adaptation: (a) Scaling parameter based on the local HU values; (b) constitutive law behaviour showing radial strain against the pressure for the trachea and larger and small bronchi.

HU values up to 500, it is assumed that the airway lumena are not entirely blocked by fluid. Although airway plugging could be easily included if required. The resistance at each terminal sub-region at generation 23 is updated to be $R_{new} = R * S$. The contribution of lung compliance in the lumped model is estimated to change using $C_{new} = C/S$. This means the expiratory time constant of each terminal sub-region $RC_{exp} = R * C = R_{new} * C_{new}$ is kept the same. Before performing the CFD analysis, the model branching is truncated in order to prevent excessively long simulation run times of the model. The network parameters of resistance and compliance are lumped together and thus re-calculated during the truncation process. As airways are in parallel, this means the resistance of the child airways (R_1 and R_2) are lumped together as:

$$\frac{1}{R_{Lumped}} = \frac{1}{R_1} + \frac{1}{R_2}, \tag{12}$$

While the two compliance values (C_1 and C_2) are lumped as:

$$C_{Lumped} = C_1 + C_2. \tag{13}$$

This means that after all airways have been truncated back to generation 14, that the expiratory time constant $R * C$ will be different for all terminal lumped models.

3. Results

A supplementary file is included with this paper showing the network generation algorithm in full, and a sensitivity analysis of all the primitive parameters in the CFD model.

3.1. Network generation algorithm

The network generation algorithm successfully filled the lung volume with airway structures. One of the algorithm's terminating conditions is a defined minimum volume percentage. If a sub-volume goes below the minimum volume threshold, then no more airways are created within that network pathway. The remainder of any further respiratory structures are contained in a terminal 0D alveolar model. Fig. 2 shows the final network generated of the mild disease case, although the graphic is limited to show only up to generation 15 due to image clarity issues. The final network produced for patient 1 (mild case) contains 1,919,861 airways up to the 23rd generation, while for the patient 2 (severe case), 1,045,691 airways where created. Fig. 6 shows the following network statistics for the generation number, Horsfield order, and Strahler number: the number of airways, the mean and standard deviation of branching angles, the mean airway diameter and length. All statistics are within the expected range from both theoretical values [13], experimental studies [14,15], and other airway

network creating algorithms [16–18]. The total volume of the lungs for the patients are vastly different, with the lung volume for patient 1 and 2 respectively, being 5452 ml and 2143 ml. The total volume of the airways of patient 1 and 2 respectively, are estimated by the network generation algorithm to be 304.09 ml and 203.48 ml. This gives the percentage of lung volume taken up by the airways to be 5.58% and 9.5% of their total lung volume, to patient 1 and 2 respectively. This is consistent with the value of approximately 8% given in [36] (92% of lung is parenchyma and the remaining 8% being other structures that included the airways). The remainder of the volume is distributed to the lung parenchyma, including alveoli, and other structures such as blood vessels.

3.2. Effect of resistance on airway waveforms

To avoid excessive computation times, the network utilised in this section is that of patient 1, and includes up to generation 14 with 25,145 airways. The remainder of the network structures, which would primarily be composed of respiratory bronchioles and alveoli, are incorporated into each terminal 0D model. The effect of changing the terminal resistances in the 14 generation network are shown in Figs. 7(a), and 7(c). The terminal resistances include the resistance to airflow of the smaller airways, such as respiratory bronchioles and alveoli, and also the resistance to flow of the lung parenchyma and the chest wall. Due to the non-linear relationship between resistance, compliance, airflow, and pressure, it is difficult to truly separate the effects of resistance and compliance as they are implicitly linked. For example, increasing the resistance will increase the pressure, which in turn will change the compliance via the constitutive equation. The pressure change shown by changing the resistance is relatively minor, as seen in Fig. 7(a). This is primarily due to the fact that the contribution of the terminal resistance to the total resistance of the lung is much smaller than those located further up the tree.

An increase in resistance causes a greater pressure increase within the trachea during the initial inhalation phase, and a greater pressure drop within the trachea during the initial exhalation phase. The resistance increase causes the hysteresis of the pressure–volume (P–V) loop to be exacerbated and is shown in Fig. 7(c). If the resistance is increased the P-V loop becomes wider, and when the resistance is reduced the P-V loop becomes narrower.

In order to analyse the effects of the resistance on the pressure waveform in the middle of the trachea, the pressure difference in the temporal domain is calculated as $\frac{\partial P}{\partial t} \Delta t$ and shown as Fig. 7(e). This allows the waveform to be broken down into smaller blocks and helps determine where the waveform shape changes as a result of the change in resistance. It is observed that the largest changes in the waveform due to a resistance change occurs primarily at 4 distinct points in
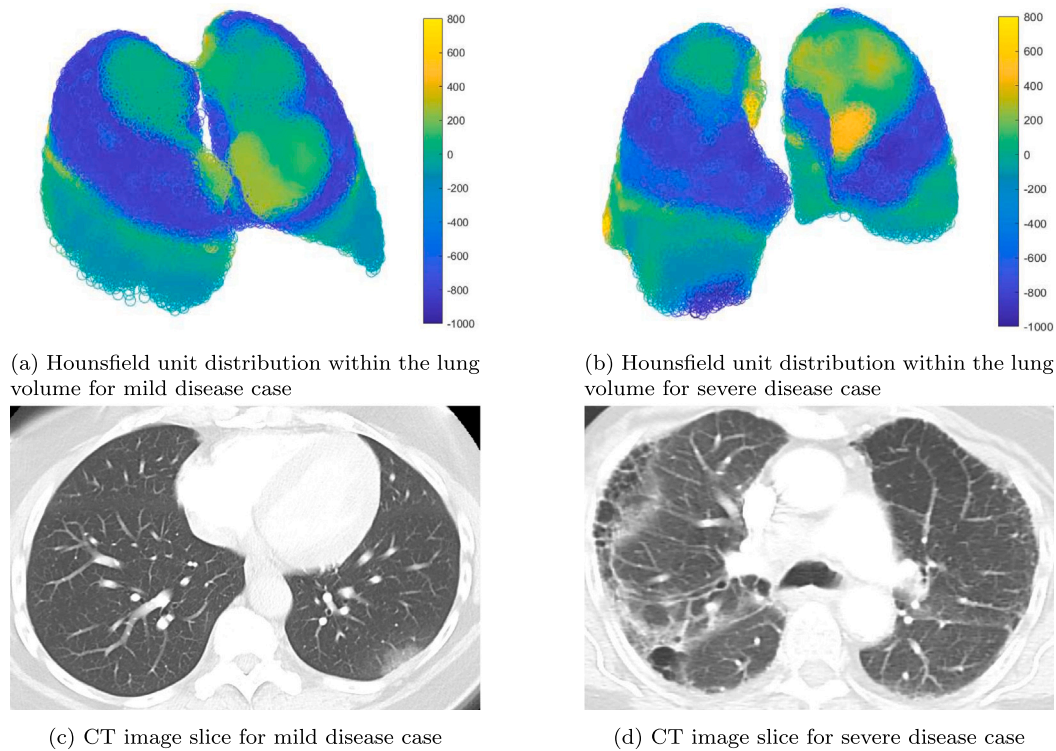
(a) Hounsfield unit distribution within the lung volume for mild disease case

(b) Hounsfield unit distribution within the lung volume for severe disease case

(c) CT image slice for mild disease case

(d) CT image slice for severe disease case

Fig. 5. Hounsfield unit distribution throughout the lungs, extracted from the patient CT images. An example CT image slice is given for each patient.

time. The first phase (time between 0–0.2 s) is during the initial ramp up phase on inhalation, which is generally the most dynamic part of the cycle, and occurs most significantly before the onset of alveoli recruitment. The second phase (time between 0.8–1.8 s) is the period between the peak pressure and the plateau pressure, which occurs in part due to the visco-elastic recoil of the lung and the re-distribution of pressure throughout the lung. The third phase (time between 1.8–2.0 s) is at the very beginning of the exhalation phase, which is most significant in the period between the start of inhalation and the beginning of alveolar air expulsion. The fourth phase (time between 3.2–3.4 s) where this occurs is another type of pressure redistribution, which occurs at the end phase of exhalation. In ventilated patients, phase 4 is often termed the auto-peep phenomena.

3.3. Effect of compliance on airway waveforms

The effect of changing total respiratory compliance on the trachea pressure and P-V loop are shown in Figs. 7(b) and 7(d), respectively. Reducing the compliance, increases both the peak and plateau pressures in the trachea. Conversely, an increase in compliance will reduce the peak and plateau pressures. In the P-V loop, a reduced compliance essentially rotates the waveform clockwise around the lowest pressure-volume point, which corresponds with the beginning of inhalation. An increase in compliance rotates the waveform anti-clockwise around the same low pressure-volume point. In order to investigate where the compliance change particularly affects the pressure waveform shape, the pressure difference in the temporal domain is also calculated for the compliance changing cases and is shown in Fig. 7(f). It can be observed that the compliance generally affects the waveform in two main phases. The first phase starts during the latter part of the inhalation ramp-up (which occurs after alveolar recruitment), and continues to impact the pressure change until the peak pressure is reached. The second phase occurs close to the beginning of exhalation and ends when the pressure reaches the defined peep pressure.

### 3.4. Analysis of COVID-19 affected lungs

Histograms showing the HU frequency distribution within each lung for both patients are shown in Fig. 8. The peaks corresponding to an −800 HU frequency are much sharper in the mild COVID case and are shown for the left and right lung in Figs. 8(a) and 8(b). This is expected, as the majority of the HU values are expected to be around −800 HU representing healthy air-filling regions of the lung. Damage or fluid in the lungs will increase the HU values in those regions. Additional features are expected within the lung: the range between −100 to 0 HU that indicates fat deposits; between 100 to 200 HU that represents muscle. A significant frequency of HU values in general between −150 to 300 HU represent body tissues and fluid filled structures. When the blood vessels are enhanced in the CT for angiography, a small peak may be present around 300–500 HU.

In the more severe disease case, shown in Figs. 8(c) and 8(d), there is a significant frequency of HU values between −700 and −100 HU. This type of histogram can represent different conditions, such as pulmonary fibrosis, pneumonia (lung inflammation), and pulmonary oedema (interstitial fluid build-up). In the patient with more severe disease, the presence of pneumonia is the primary cause for this feature in the HU frequency histogram. Another complication that can be determined from the histogram is emphysema. Emphysema occurs when the wall connecting neighbouring alveolar sacs break down, effectively joining neighbouring alveolar sacs into one larger alveolus. The effect this has on the histogram is that the sharpness of the waveform shape is reduced, particularly in the regions between −850 to −1000 HU. A small amount of HU values in this range would be expected throughout the entire lung as the larger airways would have HU values within this range, though typically this would not produce a very noticeable frequency on the histogram. The effect of emphysema is most pronounced in the right lung of the patient with more severe disease (Fig. 8(c)), with a lower incidence of emphysema also present in the left lung.
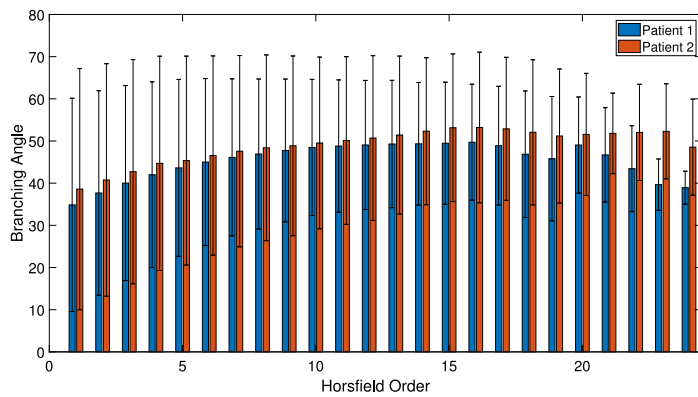
The maximum inflation of each airway branch up to and including the 12th generation, can be seen in Figs. 9(a) and 9(b) respectively.
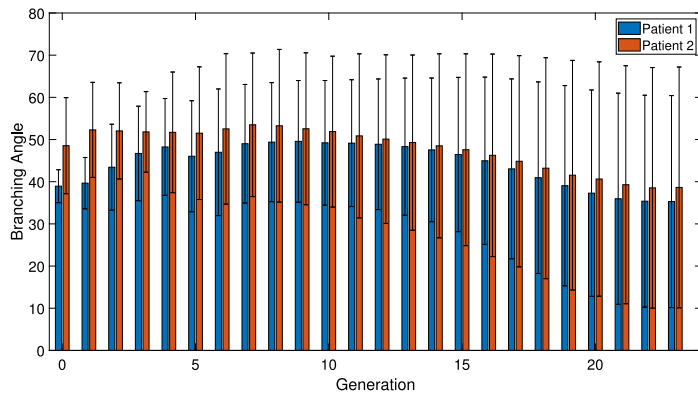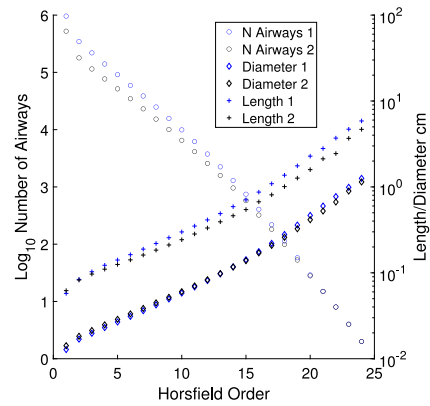
(a) Mean branching angle and standard deviation for each generation.
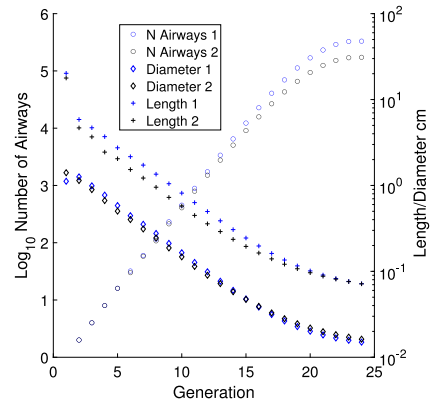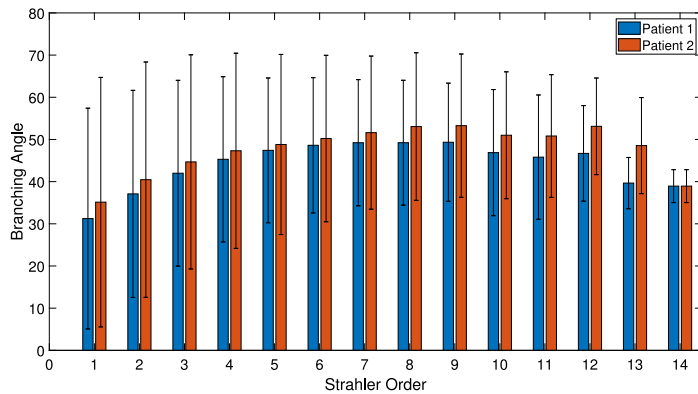

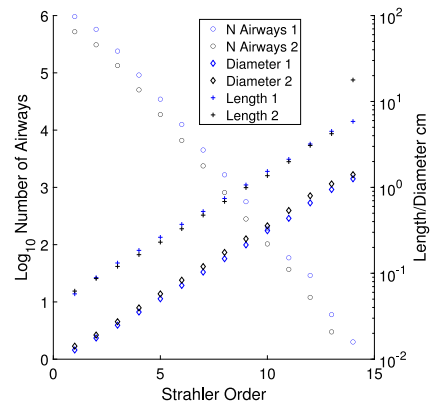(b) Total number, mean length and diameter of airways in each generation.

(c) Mean branching angle and standard deviation for Horsfield order.

(d) Total number, mean length and diameter of airways for Horsfield order.

(e) Mean branching angle and standard deviation for Strahler order.

(f) Total number, mean length and diameter of airways for Strahler order.

Fig. 6. Analysis of network generation algorithm output for patient 1 and 2. Analysis is shown for generation number, Horsfield order and Strahler order. The metrics investigated are the number of airways, branching angle, airway lengths and diameters.

The percentage change of inflation is defined as:

$$Inflation = \frac{(A_1 - A_2)}{A_1} * 100, \qquad (14)$$

where A_1 is the maximum area observed in the non-COVID-affected simulation, and A_2 is the maximum area of the COVID-affected simulation at the same location in the network. The largest increase in inflation in the mild disease case was 8.5%, while in the severe case it was 33%. Fig. 9(c) is a histogram that shows the number of airways which are over-inflated, up to and including the 12th generation (to

coincide with Figs. 9(a) and 9(b)). It is observed that the lungs severely affected by COVID-19 have a significant increase in inflation from the baseline/healthy simulation. The global inflation for this patient is observed in Fig. 9(b) and indicates the regions that undergo the largest over-inflation occur primarily, though not exclusively, in the regions affected by emphysema. Fig. 9(d) shows correlation plots of the over-inflation with the resistance at terminal airways of the network. The Spearman ρ coefficients show no correlations between the inflation and resistance in these regions. This means that analysis of the CT images,
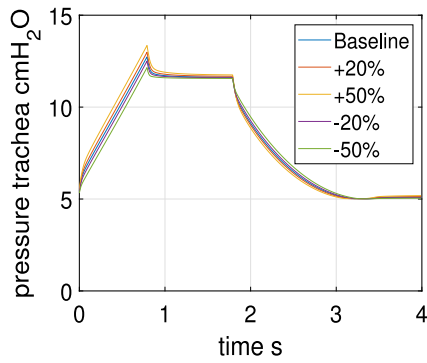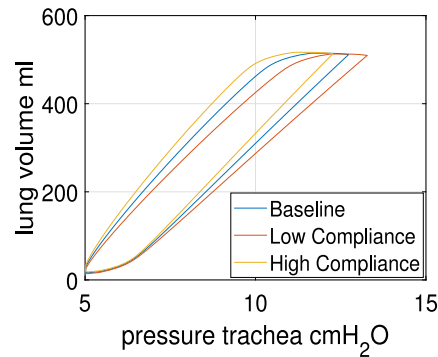
(a) Effect of changing the terminal resistance (percentage change from base simulation) to airflow on pressure waveforms in the trachea
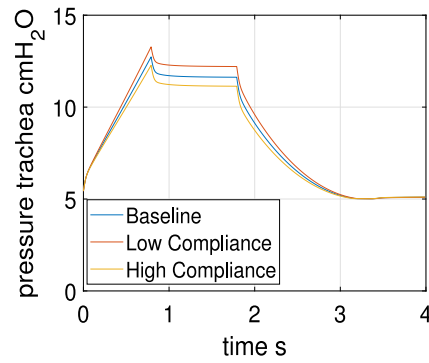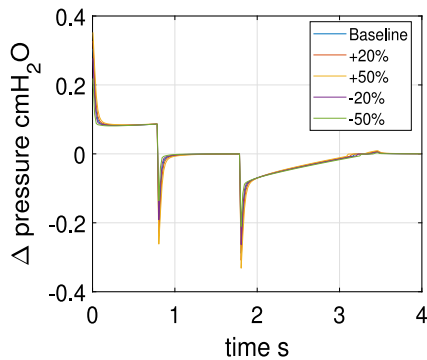
(b) Effect of changing total lung compliance on the pressure waveform in the trachea
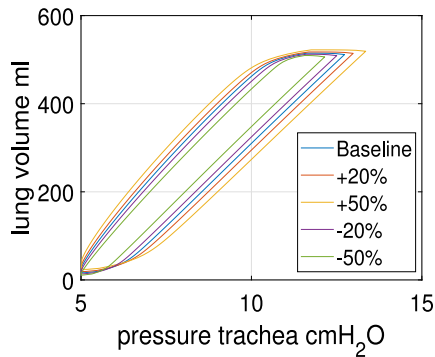
(c) Effect of changing the terminal resistance (percentage change from base simulation) to airflow on the lung pressure-volume relationship

(d) Effect of changing total respiratory compliance on the lung pressure-volume relationship

(e) Change of tracheal pressure in the temporal domain and the effect of changing resistance
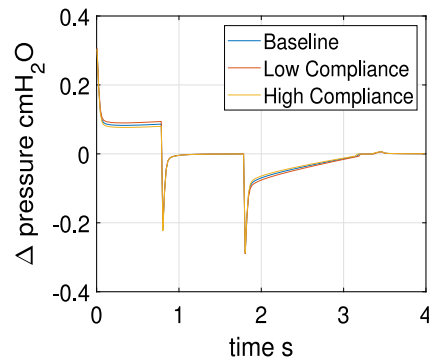
(f) Change of tracheal pressure in the temporal domain and the effect of changing compliance

Fig. 7. Comparison of different waveforms produced by the model with changes to the terminal resistance (resistance that represents the respiratory bronchioles and alveoli) and total lung compliance.

which have been used to estimate the resistance and compliance distribution in the lung, is not sufficient to estimate the functional impact of the on the lung (pressure, flow distribution, and inflation).

4. Discussion

The network generation algorithm used in this work used a bottom-up approach with a purely deterministic approach to fill the lung. This is primarily as one of the fundamental assumptions of the algorithm already provides an estimated airflow distribution by virtue of its more controllable resistance distribution. The network generation algorithm was limited to a minimum sub-volume to avoid excessive computational run times and memory requirements for both the network generation algorithm and its proceeding CFD simulations. The network generation proposed in this paper gives a similar performance of volume-filling to other published algorithms [16–18] with similar branching angles, airway diameters, airway lengths, and total number of airways.

An overview comparing different global airflow models within lung is shown in Table 2. There have been a few previously published models on full lung airflow under mechanical ventilation. One such study involved a 3D poro-elastic model to model lung pressure-volume curves [29]. In which, the first 3 generations were not explicitly modelled. Instead, the lung boundary was considered closed except at the locations where the 3rd generation airways would be located. A prescribed pressure (for pressure controlled ventilation), or flow rate (for volume-controlled ventilation), was used as a boundary condition
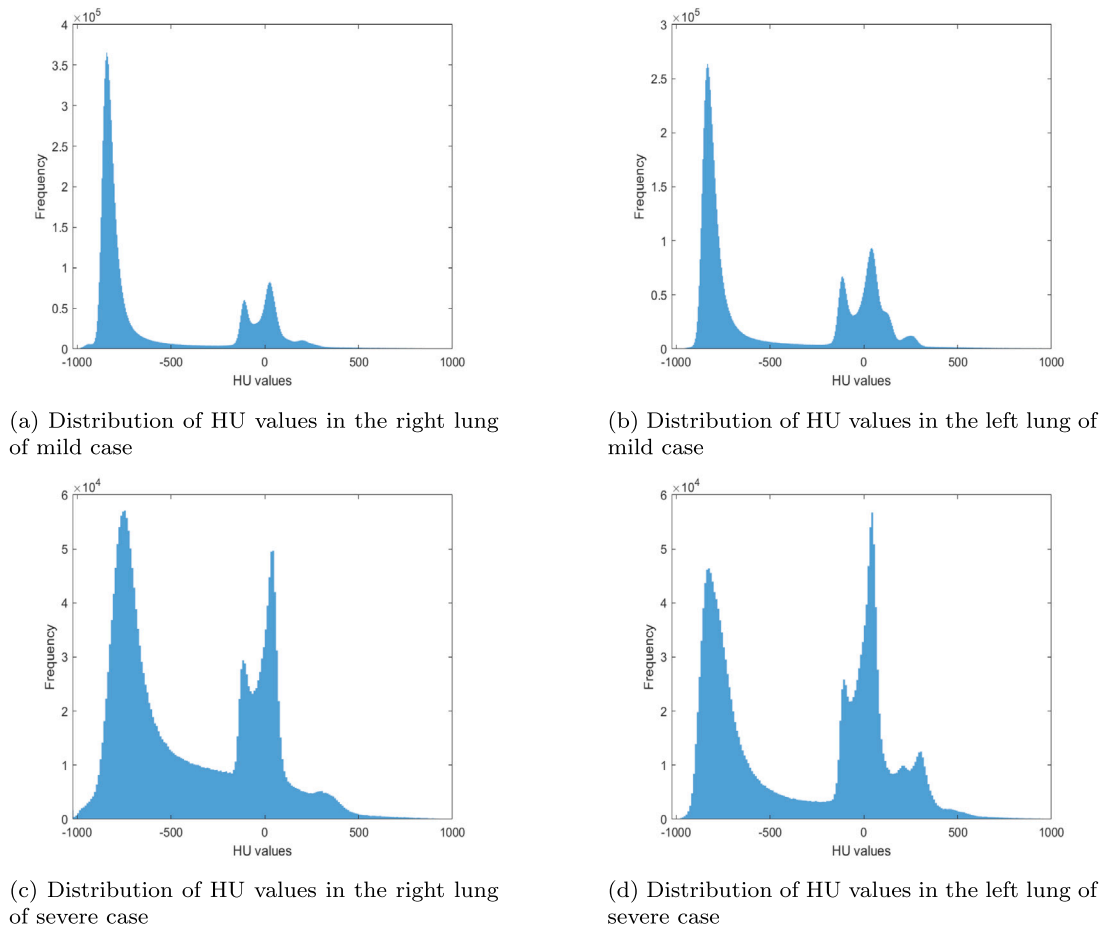
(a) Distribution of HU values in the right lung of mild case

(b) Distribution of HU values in the left lung of mild case

(c) Distribution of HU values in the right lung of severe case

(d) Distribution of HU values in the left lung of severe case

Fig. 8. Histograms of the Hounsfield unit frequency distribution of the two cases. Each lung has been analysed separately in order to highlight the asymmetry in the distribution of severity.

at these entrances to the lung at the opening left by the 3rd generation airways. The entirety of the lung was then considered a porous media with hyper-elastic, isotropic wall properties. The poro-elastic wall model showed the ability to reproduce P-V curves. However, modelling the entire lung as porous media does not represent the physiological reality as there are essentially an infinite number of pathways that air can travel between locations. Modelling the lung in this way could potentially capture global parameters and relationships, such as the pressure-volume loop. Porous media would not be able to capture locally distributed phenomena such as plugging or alveolar damage. The modelling approach proposed here was chosen due to its potential to connect local scale phenomena with global scale phenomena. This offers a versatility that can be exploited and developed further around a variety of diseases or injury mechanisms.

A 3D-0D model of airflow in the lungs was developed for spontaneous breathing [25]. The 3D modelling was added for the first few generations to overcome the shortcomings of the 0D lumped model which did not adequately capture wave reflection phenomena that occur in the upper airways. The same group also coupled their 0D lumped model with electrical impedance tomography [46]. In comparison to their methodologies, the same type of non-linear distributed 1D model presented here has been shown to capture the majority of wave-propagation phenomena in the more complex flow behaviour of the cardiovascular system when compared to 3D flow [47]. Thus 1D models are generally regarded to be a good compromise between computational power requirements and accuracy. Additionally, Several differences in the solutions of lumped models and 1D models have also been observed, particularly for sharper waveforms (higher frequency

Table 2
Comparison of the main studies involved in global respiratory modelling. The columns are as follows: turbulence model (TM) for trachea and bronchi; non-linear wave propagation (NLWP) in the upper airways (U) and lower airways (L); compliant structures (CS) in the upper airways (U), lower airways (L), and alveoli (A); breathing type (BT) that includes spontaneous breathing (S), and invasive mechanical ventilation (V); model personalisation (MP) using imaging and patient data for the airway network (N) and model parameters (P). The symbol • means the study includes the ability referred to in the column, ×mean the model does not investigate or capture it.

Study	TM	NLWP		CS			BT		MP	
		U	L	U	L	A	S	V	N	P
This study	×	•	•	•	•	•	×	•	•	•
[19]	×	×	×	×	×	×	•	×	•	×
[25]	•	•	•	×	×	•	•	×	•	×
[26]	×	×	×	•	•	•	•	×	•	×
[27]	×	•	•	×	×	•	•	×	•	•
[28]	×	×	×	×	×	•	•	×	•	•
[29]	×	×	×	•	•	•	×	•	×	•
[30]	•	•	×	•	×	•	•	×	•	•
[31]	•	•	×	×	×	•	•	×	•	×
[32]	×	•	×	×	×	•	•	×	•	×
[33]	•	•	×	•	×	×	•	×	•	•

waves) [39,48,49]. In the case of lung modelling, these higher frequency waves are more likely to occur under mechanical ventilation, specifically the peak pressure value in the pressure waveform. More complex wave-reflection phenomena are also more likely to occur in cases of disease or trauma. 1D models have been shown to be more effective than 0D models at capturing wave reflection phenomena [39].
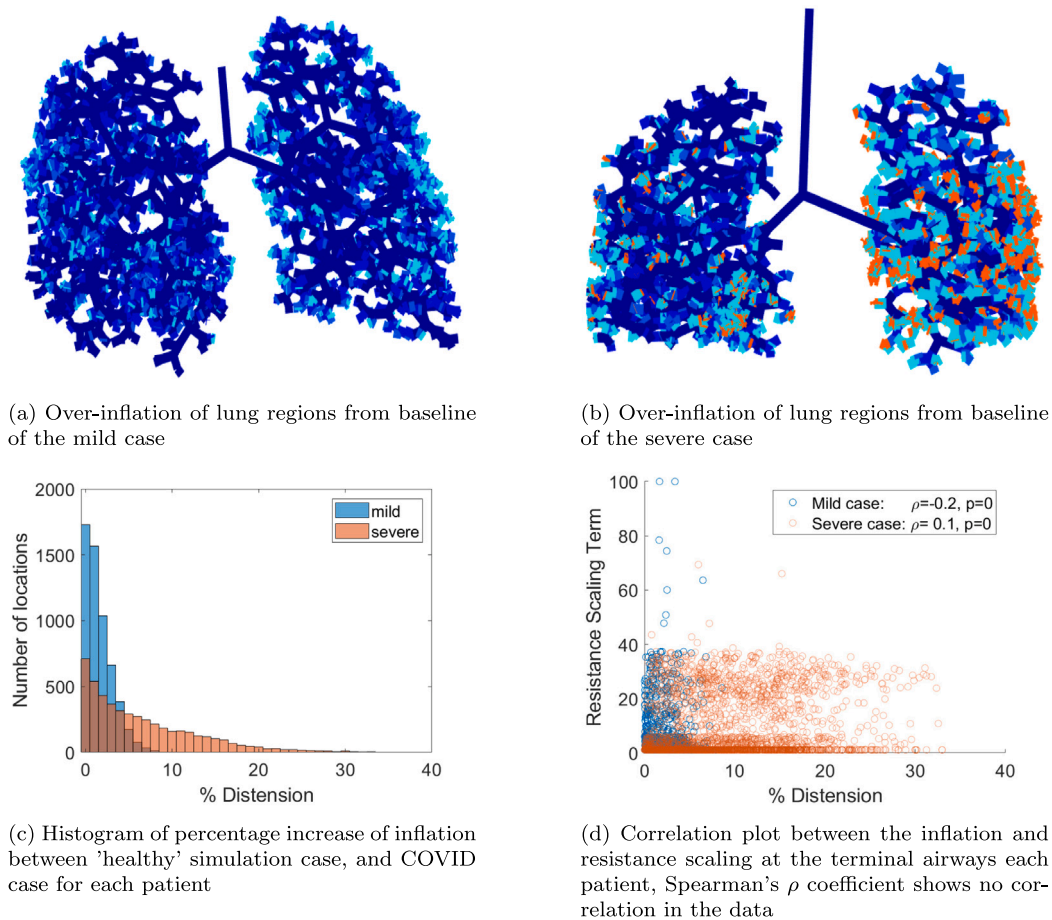
(a) Over-inflation of lung regions from baseline of the mild case

(b) Over-inflation of lung regions from baseline of the severe case

(c) Histogram of percentage increase of inflation between 'healthy' simulation case, and COVID case for each patient

(d) Correlation plot between the inflation and resistance scaling at the terminal airways each patient, Spearman's ρ coefficient shows no correlation in the data

Fig. 9. Whole lung overview of inflation change from the baseline 'healthy' case, to the COVID-affected lungs. In (a) and (b), blue indicates that the change of inflation is less than 3%, light blue indicates the change is between 3% and 10%, and red is for a change greater than 10%. The number of locations with a percentage of over-inflation is shown in the histogram plot (c). Correlation plots are shown in (d).

In physiology, under-inflated and over-inflated regions will have different densities of alveoli. An over-inflated region will have a lower alveolar density and lower HU value, while an under-inflated section would have a high HU value. To achieve over-inflation in the model, increases in compliance and decreases in resistance would be required in that lung region. The use of the scaling term in the model addresses this phenomena by increasing compliance and lowering resistance in regions with lower (more negative) HU values, and by decreasing compliance and increasing resistance in regions with higher HU values.

The model shows the expected response to the volume-controlled defined airflow waveform at the inlet. The expected pressure waveform in the trachea is achieved, which also means the shape of the pressure-volume loop is as expected [50]. The model response to both a change in resistance and of compliance is also in agreement with that given in medical literature [51]. This is the case for both waveform shapes of pressure–time, and pressure-volume. A widening of the pressure-volume loop occurs when the resistance increases, and narrows when resistance decreases. While the entire pressure-volume loop rotates towards the volume axis when the compliance increases, and towards the pressure axis when compliance decreases.

The general effect of emphysema is to increase the compliance and reduce the resistance [52]. The change in structure can also increase the risk of alveolar collapse by interfering with the surfactant distribution, although the use of peep in mechanical ventilation reduces this risk considerably. Mixed lung disease, e.g. a combination of fibrosis and emphysema, can be a particular challenge in clinical assessment [53, 54]. The effect of the higher resistance, lower compliance of fibrosis with the lower resistance, higher compliance of emphysema can cause some clinical measurements to appear normal, in particular the ratio between the forced expiratory volume in the first one second and the forced vital capacity of the lungs (FEV1/FVC ratio), Residual Volume (RV), and the RV to total lung capacity (TLC) ratio [54]. Although the global clinical measures may appear to be somewhat counterbalanced by the presence of both diseases, the patients typically have a poor prognosis as exchange of gases within the lung are severely affected. The presence of both may lead to normal global measures, however the local mechanisms and effects of both diseases are very different and thus the pressure and volume/inflation of regions of the lungs will be very different depending on which disease is present in that location. The areas affected primarily by emphysema will distend much more when there are nearby regions that are affected by fibrosis. This is due to fibrosis increasing resistance, which lowers the volume of airflow to some region, while emphysema reduces resistance, which raises the volume of airflow to another region. The presence of both diseases can interfere with airflow distributions in the lung even more than what would be expected if only one of the diseases was present. This could potentially increase the risk of rupture in emphysema-affected regions, as an even greater proportion of air will go to these regions, causing significant over-inflation of the affected alveoli.

An absence of correlation was observed between the resistance scaling term and the inflation of the terminal airways at the same location. This indicates that image analysis alone is not sufficient to estimate the functional impact of COVID-19 on the lungs and complementing it with fluid dynamics will provide further insight in the fundamental mechanisms and their effects on overall lung performance. This model could provide a basis for future work on respiratory diseases other than

COVID-19, and could potentially provide insight into the locations of alveoli in the lung which are likely to rupture for a given patient with a distribution of disease that has been extracted from medical imaging.

5. Conclusion

This study provides a bottom-up modelling methodology to analyse flow and pressure distribution within the lung of ventilated patients with COVID-19. The algorithm proposed in this work utilised the lung boundary of a real human lung, extracted by segmentation from pulmonary CT scans. The network generation algorithm successfully filled the lung with airways even in the presence of non-smooth regions of the lung boundary. The physics-based model used to analyse the airflow and pressure changes show the expected responses to the main system parameters of resistance and compliance. The model indicates that the risk of alveolar rupture during mechanical ventilation could increase if the lung is affected by two competing disease effects such as fibrosis and emphysema, which is commonly seen in COVID-19 patients. The airflow is forced from stiffer regions of the lung and into more compliant regions, thus significantly affecting the airflow distribution within local regions of the lung. The model can be used as a basis for further investigations on other respiratory diseases. With access to additional data, more personalised ventilation strategies can be tested effectively in this framework. The model can be used as a basis for investigation of other respiratory diseases in general.

6. Limitations

The current model is not capable of capturing auto-peep as the mechanical ventilator airflow output is defined, which prevents the inhalation and exhalation phases to have different total airflow volume. In order to be able to capture this, a numerical model of the mechanical ventilator would need to be incorporated into the model, which would allow the interaction of ventilator, breathing circuit, lung structures, and thoracic pressure to be included. Due to the lack of additional patient data, several aspects of the model had to be made consistent between patients. This includes: the initial estimate of compliance and resistance, and thus the constitutive law parameters for both the 1D airway models and terminal lumped parameter models; the inflow boundary condition; and that no airway was plugged, which could cut off entire regions of the lung to air and significantly impact the total lung compliance and resistance. In order to test the effect of some of these assumptions, a sensitivity analysis of the primitive variables in the model has been performed and is presented in supplementary material accompanying this paper. More personalised models would be achieved with access to data such as patient pressure-volume curves.

CRediT authorship contribution statement

Jason M. Carson: Writing – review & editing, Writing – original draft, Methodology, Investigation. **Raoul Van Loon:** Supervision. **Hari Arora:** Supervision, Funding acquisition, Conceptualization.

Declaration of competing interest

The authors declare that they have no conflict of interests.

Data availability

The processed data utilised in this work will be uploaded to https://github.com/JMC-biomed/Lung-Data. This includes: surface meshes of the lung and airway segmentations, the Hounsfield unit distribution in 3D space within the lung volume, and the outputs of the network generation algorithm, including 1D airway network and sub-volume information.

Appendix A. Supplementary data

A supplementary file accompanies this work to describe the network generation algorithm in full and a sensitivity analysis of the primitive parameters of the model.

Supplementary material related to this article can be found online at https://doi.org/10.1016/j.compbiomed.2024.109177.

References

[1] I. Djaharuddin, S. Munawwarah, A. Nurulita, M. Ilyas, N.A. Tabri, N. Lihawa, Comorbidities and mortality in COVID-19 patients, Gac. Sanit. 35 (2021) S530–S532, http://dx.doi.org/10.1016/j.gaceta.2021.10.085.

[2] S.A.M. van Kessel, T.C.O. Hartman, P.L.B.J. Lucassen, C.H.M. van Jaarsveld, Post-acute and long-COVID-19 symptoms in patients with mild diseases: a systematic review, Fam. Pract. 39 (1) (2021) 159–167, http://dx.doi.org/10.1093/fampra/cmab076.

[3] D.T.W. Lui, C.H. Lee, W.S. Chow, A.C.H. Lee, A.R. Tam, P. Pang, T.Y. Ho, C.H.Y. Fong, C.Y. Law, E.K.H. Leung, K.K.W. To, K.C.B. Tan, Y.C. Woo, C.W. Lam, I.F.N. Hung, K.S.L. Lam, Long COVID in patients with mild to moderate disease: Do thyroid function and autoimmunity play a role? Endocr. Pract. 27 (9) (2021) 894–902, http://dx.doi.org/10.1016/j.eprac.2021.06.016.

[4] R.A. Grant, L. Morales-Nebreda, N.S. Markov, S. Swaminathan, M. Querrey, E.R. Guzman, D.A. Abbott, H.K. Donnelly, A. Donayre, I.A. Goldberg, Z.M. Klug, N. Borkowski, Z. Lu, H. Kihshen, Y. Politanska, L. Sichizya, M. Kang, A. Shilatifard, C. Qi, J.W. Lomasney, A.C. Argento, J.M. Kruser, E.S. Malsin, C.O. Pickens, S.B. Smith, J.M. Walter, A.E. Pawlowski, D. Schneider, P. Nannapaneni, H. Abdala-Valencia, A. Bharat, C.J. Gottardi, G.R.S. Budinger, A.V. Misharin, B.D. Singer, R.G. Wunderink, Circuits between infected macrophages and T cells in SARS-CoV-2 pneumonia, Nature 590 (7847) (2021) 635–641, http://dx.doi.org/10.1038/s41586-020-03148-w.

[5] H. Wunsch, Mechanical ventilation in COVID-19: Interpreting the current epidemiology, Am. J. Respir. Crit. Care Med. 202 (1) (2020) 1–4, http://dx.doi.org/10.1164/rccm.202004-1385ed.

[6] S. Weerakkody, H. Montgomery, Should we treat COVID-19 lung injury like ARDS? Exploring the paradigm, Exp. Physiol. 107 (7) (2021) 747–748, http://dx.doi.org/10.1113/ep090010.

[7] J.N. Cronin, L. Camporota, F. Formenti, Mechanical ventilation in COVID-19: A physiological perspective, Exp. Physiol. 107 (7) (2021) 683–693, http://dx.doi.org/10.1113/ep089400.

[8] G.D. Perkins, K. Couper, B. Connolly, J.K. Baillie, J.M. Bradley, P. Dark, A.D. Soyza, E. Gorman, A. Gray, L. Hamilton, N. Hart, C. Ji, R. Lall, N. McGowan, S. Regan, A.K. Simonds, E. Skilton, N. Stallard, E. Stimpson, J. Yeung, D.F. McAuley, RECOVERY- respiratory support: Respiratory strategies for patients with suspected or proven COVID-19 respiratory failure; continuous positive airway pressure, high-flow nasal oxygen, and standard care: A structured summary of a study protocol for a randomised controlled trial, Trials 21 (1) (2020) http://dx.doi.org/10.1186/s13063-020-04617-3.

[9] H. Arora, A. Nila, K. Vitharana, J.M. Sherwood, T.-T.N. Nguyen, A. Karunaratne, I.K. Mohammed, A.J. Bodey, P.J. Hellyer, D.R. Overby, R.C. Schroter, D. Hollis, Microstructural consequences of blast lung injury characterized with digital volume correlation, Front. Mater. 4 (2017) http://dx.doi.org/10.3389/fmats.2017.00041.

[10] H. Arora, R. Mitchell, R. Johnston, M. Manolesos, D. Howells, J. Sherwood, A. Bodey, K. Wanelik, Correlating local volumetric tissue strains with global lung mechanics measurements, Materials 14 (2) (2021) 439, http://dx.doi.org/10.3390/ma14020439.

[11] M. Maghsoudi-Ganjeh, C.A. Mariano, S. Sattari, H. Arora, M. Eskandari, Developing a lung model in the age of COVID-19: A digital image correlation and inverse finite element analysis framework, Front. Bioeng. Biotechnol. 9 (2021) http://dx.doi.org/10.3389/fbioe.2021.684778.

[12] T.M. Nelson, K.A.M. Quiros, E.C. Dominguez, A. Ulu, T.M. Nordgren, M. Eskandari, Diseased and healthy murine local lung strains evaluated using digital image correlation, Sci. Rep. 13 (1) (2023) http://dx.doi.org/10.1038/s41598-023-31345-w.

[13] E.R. Weibel, Morphometry of the Human Lung, Springer Berlin Heidelberg, 1963, http://dx.doi.org/10.1007/978-3-642-87553-3.

[14] K. Horsfield, G. Cumming, Morphology of the bronchial tree in man, J. Appl. Physiol. 24 (3) (1968) 373–383, http://dx.doi.org/10.1152/jappl.1968.24.3.373.

[15] K. Horsfield, Diameters, generations, and orders of branches in the bronchial tree, J. Appl. Physiol. 68 (2) (1990) 457–461, http://dx.doi.org/10.1152/jappl.1990.68.2.457.

[16] H. Kitaoka, R. Takaki, B. Suki, A three-dimensional model of the human airway tree, J. Appl. Physiol. 87 (6) (1999) 2207–2217, http://dx.doi.org/10.1152/jappl.1999.87.6.2207.

[17] S. Montesantos, I. Katz, M. Pichelin, G. Caillibotte, The creation and statistical evaluation of a deterministic model of the human bronchial tree from HRCT images, PLoS One 11 (12) (2016) e0168026, http://dx.doi.org/10.1371/journal.pone.0168026.

[18] M.H. Tawhai, A.J. Pullan, P.J. Hunter, Generation of an anatomically based three-dimensional model of the conducting airways, Ann. Biomed. Eng. 28 (7) (2000) 793–802, http://dx.doi.org/10.1114/1.1289457.

[19] R. Bordas, C. Lefevre, B. Veeckmans, J. Pitt-Francis, C. Fetita, C.E. Brightling, D. Kay, S. Siddiqui, K.S. Burrowes, Development and analysis of patient-based complete conducting airways models, PLoS One 10 (12) (2015) e0144105, http://dx.doi.org/10.1371/journal.pone.0144105.

[20] S. Choi, S. Miyawaki, C.-L. Lin, A feasible computational fluid dynamics study for relationships of structural and functional alterations with particle depositions in severe asthmatic lungs, Comput. Math. Methods Med. 2018 (2018) 1–12, http://dx.doi.org/10.1155/2018/6564854.

[21] S. Nousias, E.I. Zacharaki, K. Moustakas, AVATREE: An open-source computational modelling framework modelling anatomically valid airway TREE conformations, PLoS One 15 (4) (2020) e0230259, http://dx.doi.org/10.1371/journal.pone.0230259.

[22] P. Nithiarasu, O. Hassan, K. Morgan, N.P. Weatherill, C. Fielder, H. Whittet, P. Ebden, K.R. Lewis, Steady flow through a realistic human upper airway geometry, Internat. J. Numer. Methods Fluids 57 (5) (2008) 631–651, http://dx.doi.org/10.1002/fld.1805.

[23] W. Faizal, N. Ghazali, C. Khor, I.A. Badruddin, M. Zainon, A.A. Yazid, N.B. Ibrahim, R.M. Razi, Computational fluid dynamics modelling of human upper airway: A review, Comput. Methods Programs Biomed. 196 (2020) 105627, http://dx.doi.org/10.1016/j.cmpb.2020.105627.

[24] L. Chen, X. Zhao, Characterization of air flow and lung function in the pulmonary acinus by fluid-structure interaction in idiopathic interstitial pneumonias, PLoS One 14 (3) (2019) e0214441, http://dx.doi.org/10.1371/journal.pone.0214441.

[25] M. Ismail, A. Comerford, W.A. Wall, Coupled and reduced dimensional modeling of respiratory mechanics during spontaneous breathing, Int. J. Numer. Methods Biomed. Eng. 29 (11) (2013) 1285–1305, http://dx.doi.org/10.1002/cnm.2577.

[26] H. Ma, H. Fujioka, D. Halpern, D.P. Gaver, Surfactant-mediated airway and acinar interactions in a multi-scale model of a healthy lung, Front. Physiol. 11 (2020) http://dx.doi.org/10.3389/fphys.2020.00941.

[27] S. Choi, S. Yoon, J. Jeon, C. Zou, J. Choi, M.H. Tawhai, E.A. Hoffman, R. Delvadia, A. Babiskin, R. Walenga, C.-L. Lin, 1D network simulations for evaluating regional flow and pressure distributions in healthy and asthmatic human lungs, J. Appl. Physiol. 127 (1) (2019) 122–133, http://dx.doi.org/10.1152/japplphysiol.00016.2019.

[28] S. Middleton, E. Dimbath, A. Pant, S.M. George, V. Maddipati, M.S. Peach, K. Yang, A.W. Ju, A. Vahdati, Towards a multi-scale computer modeling workflow for simulation of pulmonary ventilation in advanced COVID-19, Comput. Biol. Med. 145 (2022) 105513, http://dx.doi.org/10.1016/j.compbiomed.2022.105513.

[29] N. Avilés-Rojas, D.E. Hurtado, Whole-lung finite-element models for mechanical ventilation and respiratory research applications, Front. Physiol. 13 (2022) http://dx.doi.org/10.3389/fphys.2022.984286.

[30] N.D. Khoa, S. Li, N.L. Phuong, K. Kuga, H. Yabuuchi, K. Kan-O, K. Matsumoto, K. Ito, Computational fluid-particle dynamics modeling of ultrafine to coarse particles deposition in the human respiratory system, down to the terminal bronchiole, Comput. Methods Programs Biomed. 237 (2023) 107589, http://dx.doi.org/10.1016/j.cmpb.2023.107589.

[31] H. Sadafi, N. Monshi Tousi, W. De Backer, J. De Backer, Validation of computational fluid dynamics models for airway deposition with SPECT data of the same population, Sci. Rep. 14 (1) (2024) http://dx.doi.org/10.1038/s41598-024-56033-1.

[32] O.J. Ilegbusi, A. Islam, A.P. Santhanam, Computational modelling of airflow in distal airways using hybrid lung model, Math. Comput. Model. Dyn. Syst. 29 (1) (2023) 186–207, http://dx.doi.org/10.1080/13873954.2023.2243087.

[33] F. Jiang, T. Hirano, C. Liang, G. Zhang, K. Matsunaga, X. Chen, Multi-scale simulations of pulmonary airflow based on a coupled 3D-1D-0D model, Comput. Biol. Med. 171 (2024) 108150, http://dx.doi.org/10.1016/j.compbiomed.2024.108150.

[34] J. Carson, M. Lewis, D. Rassi, R.V. Loon, A data-driven model to study utero-ovarian blood flow physiology during pregnancy, Biomech. Model. Mechanobiol. 18 (4) (2019) 1155–1176, http://dx.doi.org/10.1007/s10237-019-01135-3.

[35] M.S. Olufsen, Structured tree outflow condition for blood flow in larger systemic arteries, Am. J. Physiol. Heart Circ. Physiol. 276 (1) (1999) H257–H268, http://dx.doi.org/10.1152/ajpheart.1999.276.1.h257.

[36] M. Ochs, J.R. Nyengaard, A. Jung, L. Knudsen, M. Voigt, T. Wahlers, J. Richter, H.J. rgen G. Gundersen, The number of alveoli in the human lung, Am. J. Respir. Crit. Care Med. 169 (1) (2004) 120–124, http://dx.doi.org/10.1164/rccm.200308-1107oc.

[37] S. Sattari, C.A. Mariano, M. Eskandari, Biaxial mechanical properties of the bronchial tree: Characterization of elasticity, extensibility, and energetics, including the effect of strain rate and preconditioning, Acta Biomater. 155 (2023) 410–422, http://dx.doi.org/10.1016/j.actbio.2022.10.047.

[38] J. Carson, R.V. Loon, An implicit solver for 1D arterial network models, Int. J. Numer. Methods Biomed. Eng. 33 (7) (2016) e2837, http://dx.doi.org/10.1002/cnm.2837.

[39] J.M. Carson, Development of a Cardiovascular and Lymphatic Network Model During Human Pregnancy (Ph.D. thesis), Swansea University, 2019, http://dx.doi.org/10.23889/suthesis.50058.

[40] S. Benito, F. Lemaire, B. Mankikian, A. Harf, Total respiratory compliance as a function of lung volume in patients with mechanical ventilation, Intensive Care Med. 11 (2) (1985) 76–79, http://dx.doi.org/10.1007/bf00254778.

[41] M. Hackx, D. Francotte, T.S. Garcia, A.V. Muylem, M. Walsdorff, P.A. Gevenois, Effect of total lung capacity, gender and height on CT airway measurements, Br. J. Radiol. 90 (1076) (2017) 20160898, http://dx.doi.org/10.1259/bjr.20160898.

[42] J. Lee, R. Chan, SU-E-J-171: Variation of the hounsfield unit on CT scanning parameters and reconstruction and its effect on dose calculations, Med. Phys. 40 (6Part9) (2013) http://dx.doi.org/10.1118/1.4814383, 190–190.

[43] B. Zurl, R. Tiefling, P. Winkler, P. Kindl, K. Kapp, Hounsfield units variations, Strahlentherapie Onkol. 190 (1) (2013) 88–93, http://dx.doi.org/10.1007/s00066-013-0464-5.

[44] H.A. Ai, J.G. Meier, R.E. Wendt, HU deviation in lung and bone tissues: Characterization and a corrective strategy, Med. Phys. 45 (5) (2018) 2108–2118, http://dx.doi.org/10.1002/mp.12871.

[45] B. Sul, L. Flors, J. Cassani, M.J. Morris, J. Reifman, T. Altes, A. Wallqvist, Volumetric characteristics of idiopathic pulmonary fibrosis lungs: computational analyses of high-resolution computed tomography images of lung lobes, Respir. Res. 20 (1) (2019) http://dx.doi.org/10.1186/s12931-019-1189-5.

[46] C.J. Roth, T. Becher, I. Frerichs, N. Weiler, W.A. Wall, Coupling of EIT with computational lung modeling for predicting patient-specific ventilatory responses, J. Appl. Physiol. 122 (4) (2017) 855–867, http://dx.doi.org/10.1152/japplphysiol.00236.2016.

[47] N. Xiao, J. Alastruey, C.A. Figueroa, A systematic comparison between 1-D and 3-D hemodynamics in compliant arterial models, Int. J. Numer. Methods Biomed. Eng. 30 (2) (2013) 204–231, http://dx.doi.org/10.1002/cnm.2598.

[48] V. Milišić, A. Quarteroni, Analysis of lumped parameter models for blood flow simulations and their relation with 1D models, ESAIM: Math. Model. Numer. Anal. 38 (4) (2004) 613–632, http://dx.doi.org/10.1051/m2an:2004036.

[49] N. Westerhof, B.E. Westerhof, Wave transmission and reflection of waves "the myth is in their use", Artery Res. 6 (1) (2012) 1, http://dx.doi.org/10.1016/j.artres.2012.01.004.

[50] E. Emrath, The basics of ventilator waveforms, Curr. Pediatr. Rep. 9 (1) (2021) 11–19, http://dx.doi.org/10.1007/s40124-020-00235-4.

[51] J.X. Lian, Understanding ventilator waveforms—and how to use them in patient care, Nurs. Crit. Care 4 (1) (2009) 43–55, http://dx.doi.org/10.1097/01.ccn.0000343236.47814.d8.

[52] M.V. Szabari, H. Parameswaran, S. Sato, Z. Hantos, E. Bartolák-Suki, B. Suki, Acute mechanical forces cause deterioration in lung structure and function in elastase-induced emphysema, Am. J. Physiol. Lung Cellular Mol. Physiol. 303 (7) (2012) L567–L574, http://dx.doi.org/10.1152/ajplung.00217.2012.

[53] V. Cottin, Combined pulmonary fibrosis and emphysema: bad and ugly all the same? Eur. Respir. J. 50 (1) (2017) 1700846, http://dx.doi.org/10.1183/13993003.00846-2017.

[54] R. Hage, F. Gautschi, C. Steinack, M.M. Schuurmans, Combined pulmonary fibrosis and emphysema (CPFE) clinical features and management, Int. J. Chronic Obstruct. Pulm. Dis. 16 (2021) 167–177, http://dx.doi.org/10.2147/copd.s286360.